

Pedestal density fluctuation dynamics during the inter-ELM cycle in DIII-D^{a)}

Z. Yan,^{1,b)} G. R. McKee,¹ R. J. Groebner,² P. B. Snyder,² T. H. Osborne,² M. N. Beurskens,³ and K. H. Burrell²

¹University of Wisconsin-Madison, 1500 Engineering Dr., Madison, Wisconsin 53706, USA

²General Atomics, PO Box 85608, San Diego, California 92186-5608, USA

³EURATOM/CCFE Fusion Association, Culham Science Centre, Abingdon OX 14 3DB, United Kingdom

(Received 15 December 2010; accepted 13 April 2011; published online 26 May 2011)

Detailed 2D measurements of long-wavelength density fluctuations in the pedestal region with beam emission spectroscopy during the period between edge localized modes (ELMs) indicate two distinct bands of fluctuations propagating in opposite poloidal directions in the plasma frame: one lower frequency band (50–150 kHz) advects in the ion-diamagnetic drift direction (ion mode) and a higher frequency band (200–400 kHz) advects in the electron diamagnetic drift direction (electron mode). The ion mode amplitude is modulated with the ELM cycle: it increases rapidly after an ELM and then saturates, similar to the evolution of the pedestal electron pressure and density gradients. The electron mode, in contrast, has no significant time evolution between ELMs. The decorrelation time of the ion mode is $< 5 \mu\text{s}$ [$\tau_c(c_s/a) \leq 1$], the radial correlation length is of order $10 \rho_i$ and has poloidal wave-number $k_\theta \rho_i \sim 0.1$, and the mode advects at near the ion diamagnetic velocity in the plasma frame. These spatiotemporal dynamics are qualitatively similar to features predicted for kinetic ballooning modes. © 2011 American Institute of Physics. [doi:10.1063/1.3590936]

I. INTRODUCTION

The observation of high performance (H-mode) plasmas with a spontaneously generated edge transport barrier (pedestal) is of great significance for the performance of future burning plasma experiments. Core confinement is closely correlated with the pressure at the top of the pedestal (pedestal height). For decades, theories and experiments have been focused on studies of the formation of the pedestal structure and understanding the underlying transport. Through the development of the peeling-ballooning (P-B) mode theory,¹ with P-B modes driven by a sharp pressure gradient and bootstrap current density in the pedestal, and their numerical implementation in codes such as ELITE,^{2,3} a robust prediction of edge MHD instability limits is possible for existing and future tokamaks. The recently developed EPED1 model,⁴ which is based on the hypothesis that the pedestal height is limited by the P-B instability and the pedestal width is constrained by kinetic ballooning modes (KBMs), has successfully predicted the pedestal height and width in several experiments.^{5,6} However, experimental tests of the instabilities underlying these theories are still lacking. There have been few experimental reports of pedestal turbulence properties and dynamics, which require high spatial and time resolution of the local turbulence. Providing an initial characterization of the experimental properties of pedestal turbulence and qualitative comparison with theoretical expectations is the primary goal of this paper.

We summarize our recent experimental studies of long wavelength density fluctuation characteristics and dynamics, obtained with beam emission spectroscopy (BES) measure-

ments in Type-I edge localized mode (ELMing) discharges on the DIII-D tokamak. Two bands of density fluctuations are observed propagating in opposite poloidal direction in the plasma frame, with the lower frequency band (50–150 kHz) propagating in the ion diamagnetic direction and the higher frequency band (200–400 kHz) propagating in the electron diamagnetic direction. This dual band structure is observed to be localized to the pedestal region and has a ρ^* dependence. The higher frequency fluctuation band amplitude is an order of magnitude lower than that for the lower frequency band and does not change significantly with time during the ELM cycle. The lower frequency density fluctuation band amplitude builds up quickly, within a few ms (\sim first 20% of ELM cycle) after an ELM crash, which is consistent with the pedestal electron pressure and density gradient time evolution. After that the turbulence stays quasi-stationary for > 10 ms before the onset of the next ELM. The integrated fluctuation amplitude over 50–150 kHz increases with ρ^* , while the radial correlation length of the turbulence does not vary with ρ^* . The decorrelation rate for the lower frequency band is found to exceed the local $E \times B$ shearing rate.

The experimental characteristics of the observed pedestal turbulence will be compared with predictions of theoretical models. An instability that is often invoked to explain limits to pedestal pressure gradients is the KBM. Based on linear theory, KBMs are long-wavelength instabilities that propagate in the ion diamagnetic direction in the plasma frame. The associated ion turbulence is expected to have a correlation length of tens of ion gyroradii, and can be expected to couple to the pedestal width (thus having radial and poloidal scales of a few cm for typical DIII-D pedestal conditions). KBMs are driven by and limit the pedestal pressure gradient at a value near the KBM critical gradient. They

^{a)}Paper G12 4, Bull. Am. Phys. Soc. 55, 107 (2010).

^{b)}Invited speaker.

exhibit linear growth rates that increase rapidly once a critical pressure gradient is reached, thereby matching and exceeding the large local $E \times B$ shearing rate, which is thought to stabilize most long-wavelength electrostatic drift-wave type turbulence in the H-mode pedestal.^{7,8} We note that several experimentally observed features for the lower frequency band turbulence are qualitatively similar to those predicted for the KBM.

The organization of this paper is as follows. In Sec. II, we briefly describe the experimental setup. In Sec. III, we show the characteristics of the long wavelength pedestal density fluctuations. In Sec. IV, we describe the dynamics of the pedestal turbulence evolution in between ELMs, and lastly in Sec. V, we discuss and summarize our results.

II. EXPERIMENTAL SETUP

The experiments described here are carried out on the DIII-D tokamak. The main objective was to perform a normalized toroidal ion Larmor radius ρ^* ($\rho^* = \rho_1/a \sim (T_i^{1/2}/aB_T)^{1/2}$, where “a” is the minor radius) scan on both JET and DIII-D to examine the pedestal width dependence on ρ^* . The experiments were carefully designed and performed to keep the other dimensionless parameters nearly constant at the pedestal top during the ρ^* scan.^{9,10} These parameters include: collisionality ν^* ($\propto n_{\text{ped}}/T_{\text{ped}}^2$), safety factor q_{95} (number of toroidal transits of a magnetic field line per poloidal transit at $r/a = 0.95$), Mach number M [ratio of toroidal velocity to sound speed, $M = 10^{-4} V_T/(T_i/m)^{1/2}$ $M = 10^{-4} V_T/(T_i/m)^{1/2}$], electron to ion temperature ratio T_e/T_i and normalized pressure $\beta^{\text{ped}} = p^{\text{ped}}/(B_T^2/2\mu_0)$. The value of ρ^* is scanned by a factor of two from $\sim 0.4\%$ to $\sim 0.8\%$ in the DIII-D tokamak. A detailed description of the experimental operation can also be found in Ref. 9.

Figure 1 shows the time history of several experimental parameters: current, toroidal field, density, $\beta_N = \beta a B/I_p$ (I_p is plasma current) and q_{95} . The toroidal field is scanned through three values: -2.1 T, -1.37 T, and -1.0 T, to perform the ρ^* scan. The discharges are quasi-stationary during the Type-I ELMing phase after 2000 ms. A 5×6 2D array of high sensitivity BES channels is deployed across the ped-

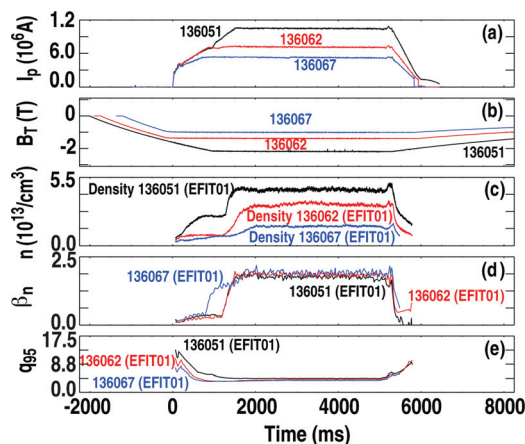


FIG. 1. (Color online) Basic parameters: (a) current, (b) toroidal field, (c) electron density, (d) β_N , and (e) q_{95} in the experiment.

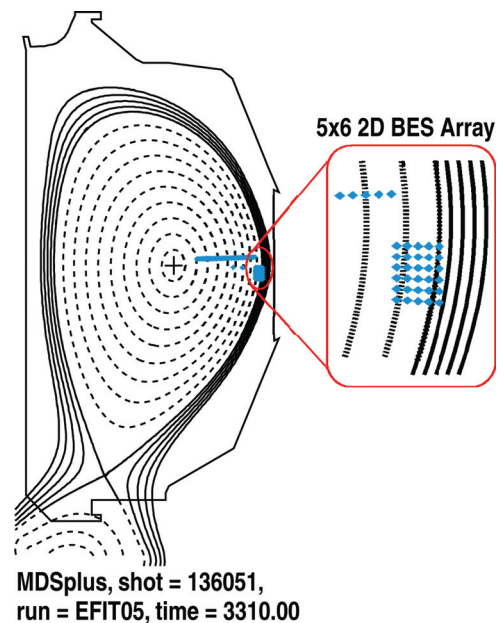


FIG. 2. (Color online) Equilibrium of plasma from EFIT with BES diagnostic image locations overlaid.

estal region from $r/a \sim 0.88$ to $r/a \sim 1.0$ as shown in Fig. 2 to provide long wavelength density fluctuation measurements. BES measures the Doppler shifted D_α fluorescence of the heating neutral beam to investigate localized density fluctuations. The D_α light emission is correlated with the density fluctuation amplitude through atomic physics of the beam excitation process.^{11,12} Each channel images an approximately 0.8 cm (radially) by 1.2 cm (poloidally) region near the outboard midplane, and the channel-to-channel separation is similar. An additional 32 channel linear BES array ($\Delta R \approx 0.8$ cm) spans from $r/a \sim 0.3$ to $r/a \sim 0.88$. BES provides density fluctuation measurements with a Nyquist frequency of 500 kHz for wavenumbers $k_\perp < 3$ cm⁻¹. A detailed description of the BES diagnostic can be found elsewhere.¹³ Electron density and temperature are measured by a Thomson scattering (TS)¹⁴ system, and a charge exchange recombination (CER)¹⁵ system is used to measure ion temperature, density and rotation of fully ionized carbon; the radial electric field is calculated via the first order radial ion force balance equation for the C⁺⁶ impurity species¹⁶ via the CER measurements. Edge profiles are fitted using a hyperbolic tangent function.¹⁷

III. CHARACTERISTICS OF THE PEDESTAL DENSITY FLUCTUATIONS

The spatially and ρ^* resolved power spectra are evaluated to investigate the pedestal fluctuation properties that pertain to gradient-limiting instabilities and perhaps drive transport. The cross spectra and cross phase between two poloidally separated BES channels ($\Delta Z = 1.2$ cm) are calculated and shown in Fig. 3(c) in the Type-I ELMing phase for four different radii at $\rho^* \sim 0.4\%$. The data were averaged over the last $\sim 10\%$ of the inter-ELM window for hundreds of ELM cycles, to provide a statistical ensemble averaged measurement. The typical statistical error is about 10%. As

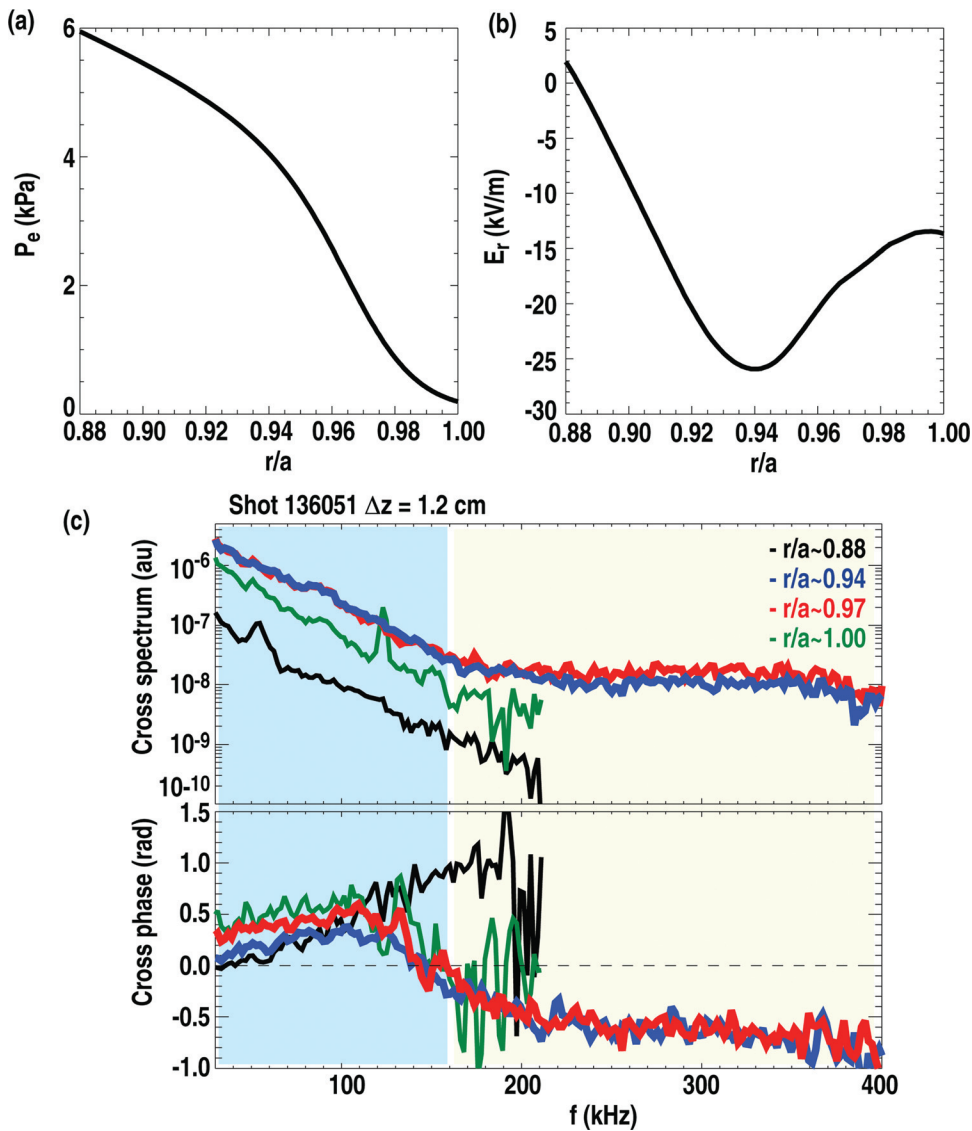


FIG. 3. (Color) (a) Electron pressure profiles, (b) radial electric field across pedestal region, and (c) poloidal cross spectrum (upper panel) and cross phase ($\Delta z = 1.2$ cm) (lower panel) of density fluctuations from BES measurements at $\rho^* \sim 0.4\%$ for four different radial locations: $r/a \sim 0.88$ (black), $r/a \sim 0.94$ (blue), $r/a \sim 0.97$ (red), and $r/a \sim 1.00$ (green). The blue region (positive cross phase) indicates turbulence propagating in the ion diamagnetic direction in the lab frame and the yellow region (negative cross phase) indicates turbulence propagating in the electron diamagnetic direction.

is shown in Fig. 3(c), two distinct bands of density fluctuations, a lower frequency band at 50 kHz–150 kHz and a higher frequency band at 200 kHz–400 kHz, are observed and found to propagate in opposite poloidal directions (indicated by the opposite sign of the cross phase angle) in the lab frame at $r/a \sim 0.94$ and 0.97 , which are, respectively, near the top and maximal pedestal electron pressure gradient location shown in Fig. 3(a). Figure 3(b) is the radial electric field profile. The dual band structure is not observed at the other two sampled locations: $r/a \sim 0.88$ and 1.00 . The amplitude of the higher frequency band is about an order of magnitude lower than that for lower frequency band. Figure 4 shows a similar cross spectrum and cross phase measurement for three different ρ^* values at $r/a \sim 0.94$. It shows the dual band structure has a ρ^* dependence as well: it is most prominent at low $\rho^* \sim 0.4\%$. The density fluctuation power increases with ρ^* . The integrated density fluctuation amplitudes over 50 kHz–150 kHz are about 1.4% ($\rho^* \sim 0.4\%$), 1.6% ($\rho^* \sim 0.6\%$), and 2.1% ($\rho^* \sim 0.8\%$). From the cross phase and vertical (poloidal) separation, the wave number is estimated to be $k_{\theta}\rho_i \sim 0.08$ for the lower frequency band,

and $k_{\theta}\rho_i \sim 0.17$ for the higher frequency band at $r/a \sim 0.94$ and $\rho^* \sim 0.4\%$. No local magnetic fluctuation measurements are available for the pedestal on DIII-D. Therefore, it cannot be determined whether these observed fluctuations are predominantly electrostatic or electromagnetic in character. The

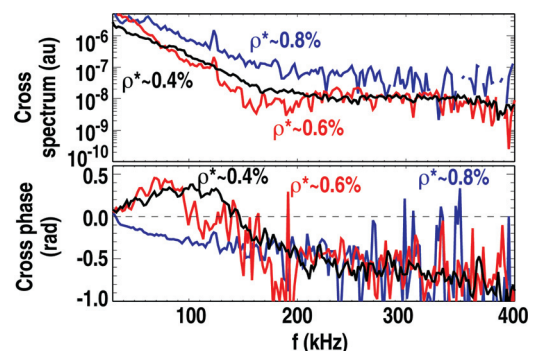


FIG. 4. (Color) Poloidal cross spectrum (upper panel) and cross phase (lower panel) of density fluctuations from BES measurements at $r/a \sim 0.94$ for three different ρ^* : $\rho^* \sim 0.4\%$ (black), $\rho^* \sim 0.6\%$ (red), and $\rho^* \sim 0.8\%$ (blue).

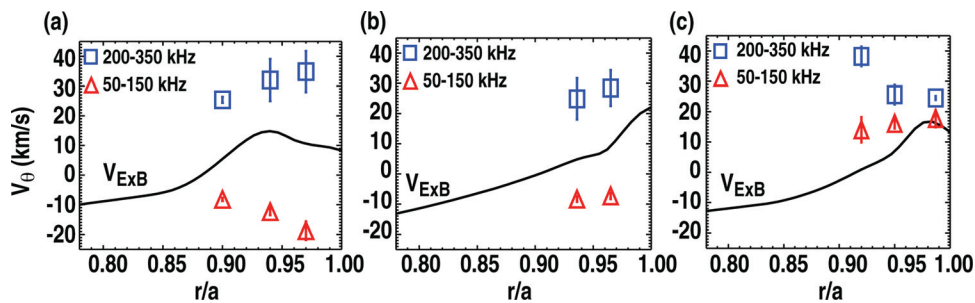


FIG. 5. (Color online) Turbulent group velocity from BES measurements for lower frequency band 50–150 kHz (triangles), higher frequency band 200–350 kHz (squares), and $E \times B$ velocity (solid line) from CER measurements for three different ρ^* values: (a) $\rho^* \sim 0.4\%$, (b) $\rho^* \sim 0.6\%$, and (c) $\rho^* \sim 0.8\%$.

integrated relative density fluctuation amplitude (\tilde{n}/n) over 50 kHz–400 kHz is a few percent, which is significantly lower than the typical edge fluctuation amplitudes in L-mode plasmas ($\tilde{n}/n \sim 10\%$).¹⁸

The poloidal turbulence group velocity for the two frequency bands is calculated from poloidally separated BES channels using multi-point time-lag cross-correlations.¹³ These poloidally separated channels are well correlated with a correlation coefficient above 0.8 at 1.2 cm poloidal spacing. In Fig. 5, the blue squares show the turbulence velocity for the 200–350 kHz (electron) band and the red triangles represent the turbulence velocity for the 50–150 kHz density fluctuation band for three different ρ^* values. Positive velocity refers to fluctuations that are propagating in the electron diamagnetic direction in the lab frame and a negative value represents propagation in the ion diamagnetic direction. The radial electric field is obtained from the radial force balance equation for the measured carbon impurity density and temperature with the CER system. The solid line in Fig. 5 is the $E \times B$ velocity calculated from these E_r profiles. It is found from comparing with the $E \times B$ velocity that the two bands do not individually match the $E \times B$ velocity at lower ρ^* when two modes are both present. The lower frequency density fluctuation band is propagating in the ion diamagnetic direction while the higher frequency density fluctuation band is propagating in the electron diamagnetic direction in the plasma frame. The difference between the turbulence velocity and the $E \times B$ velocity is a fraction of the diamagnetic drift velocity, which is typically in the range of 10–40 km/s across the pedestal region. At $\rho^* \sim 0.8\%$, there is no clear evidence that the observed mode is propagating in the ion diamagnetic direction. The 50 kHz–150 kHz frequency mode propagates with velocity nearly matching the $E \times B$ velocity. This suggests that the fluctuations observed in the lower ρ^* conditions behave differently at large ρ^* .

The decorrelation rate is shown in Fig. 6 (diamond symbols) as a function of r/a for the lower frequency band of density fluctuations during the last $\sim 10\%$ of the inter-ELM cycle at $\rho^* \sim 0.4\%$; this is calculated from the amplitude decay of the cross correlation of the poloidally separated BES channels.¹⁹ The $E \times B$ shearing rate is calculated from E_r profiles through CER measurements. It shows overall that the decorrelation rate is larger than the $E \times B$ shearing rate. This is qualitatively consistent with linear stability theory predictions for KBM. As the pressure gradient exceeds a critical value, the linear growth rate will increase rapidly and eventually exceed the $E \times B$ shearing rate.⁸ This is unlike

predictions for the ion temperature gradient (ITG) and trapped electron modes (TEMs) whose growth rates are expected to decrease with pressure gradient due to alpha-stabilization effects, and are typically well below the $E \times B$ shearing rate in the pedestal region.²⁰ Therefore, ITG and TEM are expected to be quenched by $E \times B$ shear. The fact that the decorrelation rates for the observed fluctuations are relatively high suggests that the plasma is in a regime where the KBM is expected to be unstable. However, further experiments are required to be more definitive; these will be performed in the future.

The radial and poloidal correlation functions for the lower frequency band are calculated between BES channels as a function of increasing spatial separation for three different ρ^* values as shown in Figs. 7(a) and 7(b), respectively. The correlation length is taken as the 1/e point of the correlation decay function. It shows that the radial correlation length has no significant dependence on ρ^* and the poloidal correlation length has a small dependence on ρ^* . Beurskens *et al.*¹⁰ found from the same experiment that the pedestal width has no or weak dependence on ρ^* . The similar dependence on ρ^* between the pedestal width and the observed fluctuation correlation length, as well as the similar magnitudes, suggests a link between the turbulence scale length and the size of the pedestal width.

The skewness [i.e., the third moment of the probability distribution function measuring asymmetry of the distribution of the signal, which is defined as $\tilde{n}^3 / (\tilde{n}^2)^{1.5}$] of the density fluctuations at $\rho^* \sim 0.4\%$ is computed from the BES measurements for different times after the peak of the D_α light (which indicates an ELM event) during the inter-ELM cycle, then it is time-averaged at each radial location. The fluctuation

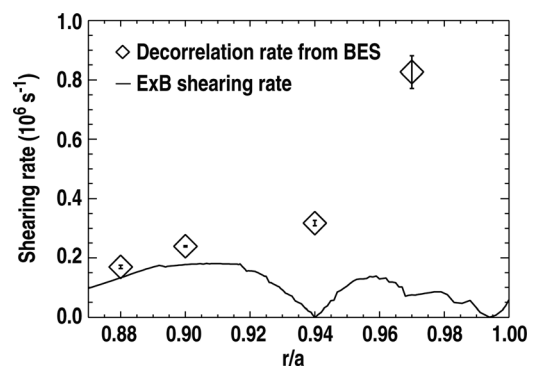


FIG. 6. Turbulence decorrelation rate profile from BES measurements (diamonds) and $E \times B$ shearing rate profile at $\rho^* \sim 0.4\%$.

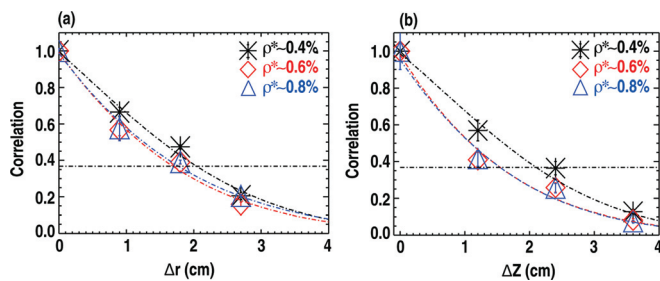


FIG. 7. (Color online) (a) Radial correlation function for lower frequency band (50–150 kHz) for three different ρ^* values; (b) Poloidal correlation function for lower frequency band (50–150 kHz) for three different ρ^* values.

data were first frequency-filtered over 50 kHz–150 kHz. The results are shown in Fig. 8. It is found that the skewness changes from negative near the pedestal top to positive near the separatrix. This indicates a predominance of negative going density events (holes) near the pedestal top and positive going density events (blobs) near the separatrix. It has been reported that there is a universal nature to bursts of outward-going blobs at the edge of the plasmas.²¹ The asymmetry of the skewness across the pedestal is consistent with the expectation that the particles move from the pedestal top outwards to the separatrix and scrape-off layer (SOL) as a result of these fluctuations. The skewness does not vary significantly with time at any of the radial locations; this contrasts with the temporal dynamics of the turbulence during the inter-ELM cycle, which suggests an increasing turbulent particle transport as the pedestal profile builds up between ELMs. However, this is a qualitative result and further analysis will be required to quantify the particle transport caused by these fluctuations.

IV. DYNAMICS OF THE PEDESTAL LONG WAVELENGTH DENSITY FLUCTUATIONS

It is predicted and generally found that the pedestal pressure evolves after an ELM crash until the onset of the next ELM in a repeating cycle. It is thus compelling to look at the fluctuation dynamics during the inter-ELM cycle and examine how they relate to the pedestal profile evolution and the underlying instabilities limiting pedestal height and gradients.

The density fluctuation spectrum measured with BES during ELMing H-mode plasmas is phase-lock averaged over successive time windows relative to the ELM time. The data

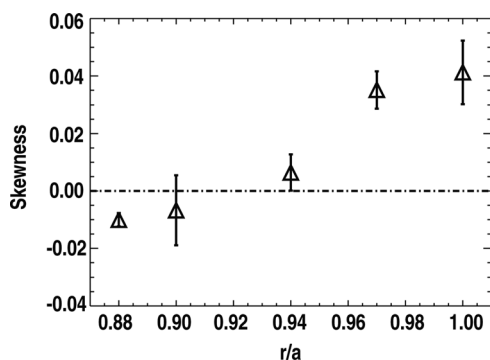


FIG. 8. Skewness of density fluctuations (50–150 kHz) from BES measurements for different radial locations at $\rho^* \sim 0.4\%$.

are averaged over more than a hundred inter-ELM windows. Figure 9 shows the density fluctuation spectrum near the maximal pedestal gradient location for different ρ^* values and different times relative to the peak of the D_α light that indicates an ELM event. It is found that the amplitude of the lower frequency band (50–150 kHz) of density fluctuations builds up quickly after an ELM crash at low ρ^* (0.4%), within a few ms., while at higher ρ^* (0.8%), it builds up more slowly, over more than 10 ms. The higher frequency (electron) band of fluctuations does not change significantly with time. We obtain the relative density fluctuation amplitude by integrating over the 50 kHz–150 kHz frequency range. Figures 10(a)–10(f) (red diamond symbols) show the ratios of the integrated density fluctuation amplitude normalized to the maximal density fluctuation amplitude $[(\tilde{n}/n)/(\tilde{n}/n)|_{\max}, \tilde{n}/n|_{\max} \approx 1.3\%]$ as a function of time after an ELM crash. It is interesting to see from the figure that there are two time scales in the evolution of the density fluctuation amplitude for $\rho^* \sim 0.4\%$ [Figs. 10(a)–10(c)] and 0.6% [Figs. 10(d)–10(f)]. First, there is a fast increase of the density fluctuation amplitude that saturates quickly within \sim a few ms with the fluctuation amplitude reaching 80% of the saturated level. Then, the evolution slows significantly with the fluctuations staying quasi-stationary before the onset of the next ELM.

The pedestal electron pressure, electron density, and electron temperature are measured with the TS system and the profiles are obtained using hyperbolic tangent fitting at the pedestal region. To look at the time evolution of the pedestal profiles, the TS data were also phase-lock averaged at different times during inter-ELM cycles. The time window used here is the same as the time window used in the fluctuation evolution calculation described above. The profile gradients are calculated at the maximal gradient location from the hyperbolic tangent profile fittings. In Figs. 10(a)–10(f), the black triangles are the pedestal electron pressure gradient, electron density, and electron temperature gradient for $\rho^* \sim 0.4\%$ [Figs. 10(a)–10(c)] and 0.6% [Figs. 10(d)–10(f)]. They are all normalized by the maximal value during the inter-ELM cycle. It shows that the pedestal profile gradients increase rapidly after an ELM crash, within a few ms, to reach $\sim 80\%$ of the maximal level, after which the evolution slows. A similar early fast recovery after an ELM crash has been previously observed in DIII-D Ref. 22 and is also observed in ASDEX Upgrade.^{23,24} The temperature evolution, in contrast, has a fast increase right after ELM crash and saturates as the electron density gradient more gradually catches up, then increases again as the electron density reaches a certain amplitude. Similar phenomenon has again been reported in ASDEX Upgrade.²⁵ Interestingly, the time evolution of the density fluctuations from BES measurements correlate most closely with the pedestal electron pressure and density gradients. This correlation suggests an interaction and coupling between the fluctuations and the electron pressure gradient. It is conjectured that the fluctuations are generated from the pressure gradient and act in turn to limit and saturate the pressure profiles and slow down any further gradient increase before the onset of the next ELM.

It is noted that KBM fluctuations would be expected to follow the pressure gradient, while ITG, for example, would

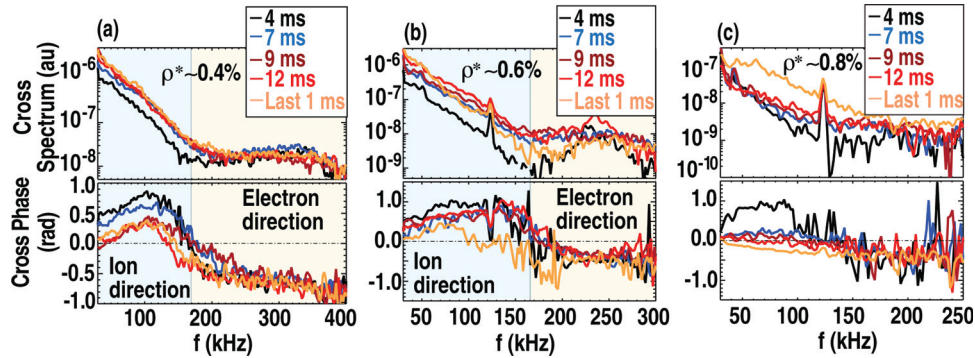


FIG. 9. (Color) Pedestal density fluctuation cross spectrum and cross phase ($\Delta Z = 1.2$ cm) for different times relative to the peak of the D_α light that indicates an ELM event at three values of ρ^* (a) $\rho^* \sim 0.4\%$, (b) $\rho^* \sim 0.6\%$, and (c) $\rho^* \sim 0.8\%$ near maximal pressure gradient location. Different colors correspond to different times after an ELM crash. The blue region (positive cross phase) indicates turbulence propagating in the ion diamagnetic direction in the lab frame and the yellow region (negative cross phase) indicates turbulence propagating in the electron diamagnetic direction.

be expected to trend oppositely, given the relatively flat temperature gradients, and increasing density gradient [reduction in η_i ($=d \ln T_i / d \ln n$)]. Unfortunately quantifying η_i would be difficult for this experiment since the CER integration time was 5 ms which would average over the time scales of interest. There is no clear consistency between the electron temperature and the time evolution of the amplitude of the lower frequency density fluctuation band, which suggests that the observed fluctuations are more connected to electron density rather than temperature.

Electron temperature gradient (ETG) mode turbulence is a plausible candidate to explain anomalous electron energy transport in the tokamak plasma edge.²⁶ To investigate this mechanism, we have estimated η_e ($=d \ln T_e / d \ln n$) at the point of maximal electron temperature gradient: it is found to be near

4.5 immediately after ELM crash and then decreases to about 2 at later times during the inter-ELM cycle for $\rho^* \sim 0.4\%$. Similar values of η_e have also been reported by ASDEX-U, DIII-D, and C-Mod.^{27–29} It is plausible that the ETG modes might be present at this magnitude of η_e and play a role in limiting the electron temperature gradient; high- k ETG modes are not observed by the BES diagnostic and we have no measurements of fluctuations at appropriate wavelengths. We note that a recent nonlinear calculation of ETG turbulence suggested that transport from ETG modes could account for the electron thermal transport in an ASDEX-U discharge.³⁰

Interestingly, we noted that there is a correlation between the higher frequency electron fluctuation band and the electron temperature gradient evolution in that both exhibit little temporal variation during the inter-ELM cycle. This might suggest that the lower-amplitude, but higher frequency electron band is driven by the electron temperature gradient. Given the lower-wavenumber fluctuation range measured by BES, this would seem more consistent with the behavior of trapped-electron mode turbulence. In the future, detailed characterization of this higher frequency electron band will be performed. It is also noted that analysis of the structure and gradients of the outer pedestal region ($0.98 < \rho < 1.0$) in some DIII-D discharges is consistent with a paleoclassical mechanism also playing a role in limiting gradients in this cooler edge region.³¹ For the $\rho^* \sim 0.8\%$ condition, the density is low and the TS data exhibits higher uncertainty. Therefore it is more difficult to obtain reliable comparisons of the pedestal profile time evolution in this condition.

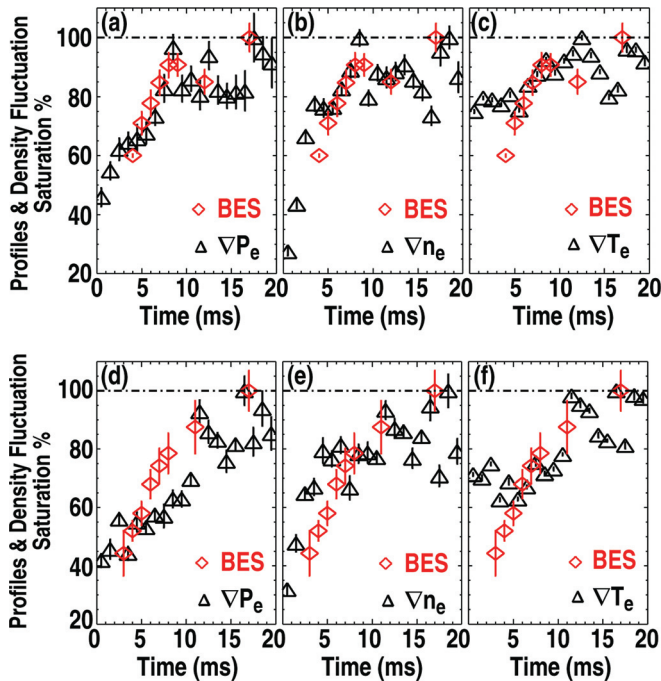


FIG. 10. (Color online) Pedestal electron pressure, electron density, and electron temperature gradients for different times relative to an ELM crash (triangles) normalized by the maximal value during the inter-ELM cycle, and the relative density fluctuation amplitude integrated over 50–150 kHz from BES measurements during the same time window normalized by the maximal value (diamonds) for (a–c) $\rho^* \sim 0.4\%$ and (d–f) $\rho^* \sim 0.6\%$.

V. SUMMARY

We have reported the characteristics of long wavelength density fluctuations obtained with BES measurements in the pedestal region during ELMing H-mode discharges. The observed dual-band fluctuations have unique spatial and ρ^* dependencies, and are most prominent near the maximal pressure gradient region and at lower $\rho^* \sim 0.4\%$. The radial and poloidal correlation lengths of the lower frequency band have no or weak dependence on ρ^* , which is consistent with previous observations that the pedestal width has no or weak dependence on ρ^* .¹⁰ The lower frequency band is observed to propagate in the ion-diamagnetic direction while the

higher frequency band propagates in the electron-diamagnetic direction in the plasma frame. The mode velocity is comparable to the diamagnetic velocity. The decorrelation rate of the lower frequency band exceeds the local $E \times B$ shearing rate. Taken together, these characteristics are all qualitatively consistent with the predictions for the KBM.^{7,8} The dynamic behavior of the lower frequency band of density fluctuations and their correlation to the pedestal pressure and density gradient suggest an interaction and coupling between these fluctuations and the pressure gradients. These fluctuations have shown a similar time history to the pedestal electron pressure gradient, growing rapidly during recovery from an ELM crash and then reaching an approximate saturation. This correlation between fluctuations and gradients would be a signature expected if KBM modes were being driven by the pressure gradient and ultimately limited the pressure gradient. However, more work is required to determine if this is the correct physics and if the observed fluctuations drive significant transport in the pedestal. We note that peeling-ballooning modes have been invoked to possibly explain some ELM instabilities in NSTX.³² This paper is more focused on the lower frequency band of density fluctuations since they have clear dynamical variation and larger amplitude. But it is noted that the higher frequency band of density fluctuations that propagate in the electron-diamagnetic direction in the plasma frame may be correlated with TEM and the dynamic behavior may be related to the electron temperature gradient. ETG mode turbulence could be expected at the observed magnitude of η_e . However further analysis and higher wavenumber measurements are needed to obtain a more definitive conclusion. Future experiments will be designed to elucidate the scaling dependencies of the pedestal turbulence characteristics, and nonlinear simulations of the pedestal are being developed to help identify the nature of these fluctuations and their role in pedestal structure and stability.

ACKNOWLEDGMENTS

This work was supported by the U.S. Department of Energy under DE-FG02-89ER53296, DE-FG02-08ER54999, DE-FC02-04ER54698, and DE-FG02-95ER54309. The authors appreciate the support of the DIII-D team and valuable discussions with Professor J. D. Callen.

¹J. W. Connor, *Plasma Phys. Controlled Fusion* **40**, 191 (1998).

²H. R. Wilson, P. B. Snyder, G. T. A. Huysmans, and R. L. Miller, *Phys. Plasmas* **9**, 1277 (2002).

³P. B. Snyder, H. R. Wilson, J. R. Ferron, L. L. Lao, A. W. Leonard, T. H. Osborne, A. D. Turnbull, D. Mossessian, M. Murakami, and X. Q. Xu, *Phys. Plasmas* **9**, 2037 (2002).

⁴P. B. Snyder, R. J. Groebner, A. W. Leonard, T. H. Osborne, and H. R. Wilson, *Phys. Plasmas* **16**, 056118 (2009).

⁵P. B. Snyder, R. J. Groebner, A. W. Leonard, T. H. Osborne, and H. R. Wilson, *Phys. Plasmas* **16**, 056118 (2008).

⁶R. J. Groebner, A. W. Leonard, P. B. Snyder, T. H. Osborne, C. F. Maggi, M. E. Fenstermacher, C. C. Petty, and L. W. Owen, *Nucl. Fusion* **49**, 085037 (2009).

⁷P. B. Snyder, Ph.D. thesis, Princeton University, 1999.

⁸P. B. Snyder and G. W. Hammett, *Phys. Plasmas* **8**, 744 (2001).

⁹M. N. A. Beurskens, T. H. Osborne, L. D. Horton, L. Frassinetti, R. Groebner, A. Leonard, P. Lomas, I. Nunes, S. Saarelma, P. B. Snyder, I. Balboa, B. Bray, K. Crombé, J. Flanagan, C. Giroud, E. Giovannozzi, M. Kempenaars, N. Kohen, A. Loarte, J. Lönroth, E. de la Luna, G. Maddison, C. Maggi, D. McDonald, G. McKee, R. Pasqualotto, G. Saibene, R. Sartori, E. R. Solano, W. Suttrop, E. Wolftrum, M. Walsh, Z. Yan, L. Zabeo, D. Zarzoso, and JET-EFDA contributors, *Plasma Phys. Controlled Fusion* **51**, 124051 (2009).

¹⁰M. N. A. Beurskens, "H-Mode Pedestal Scaling in DIII-D, AUG and JET," Invited Talk, 52nd American Physical Society-Division of Plasma Physics Meeting, Chicago (submitted to *Phys. Plasmas*).

¹¹R. J. Fonck, P. A. Duperrex, and S. F. Paul, *Rev. Sci. Instrum.* **61**, 3487 (1990).

¹²T. A. Gianakon, R. J. Fonck, J. D. Callen, R. D. Durst, and J. S. Kim, *Rev. Sci. Instrum.* **63**, 4931 (1992).

¹³G. R. McKee, R. J. Fonck, D. K. Gupta, D. J. Schlossberg, M. W. Shafer, R. L. Boivin, and W. M. Solomon, *Plasma and Fusion Research: Regular Articles 2*, S1025 (2007).

¹⁴C. L. Hsieh, B. D. Bray, and C. Liu, *Rev. Sci. Instrum.* **75**, 3897 (2004).

¹⁵W. M. Solomon, K. H. Burrell, R. Feder, A. Nagy, P. Gohil, and R. J. Groebner, *Rev. Sci. Instrum.* **79**, 10F531 (2008).

¹⁶K. H. Burrell, *Phys. Plasmas* **4**, 1499 (1997).

¹⁷R. J. Groebner and T. H. Osborne, *Phys. Plasmas* **5**, 1800 (1998).

¹⁸G. R. McKee, C. C. Petty, R. E. Waltz, C. Fenzi, R. J. Fonck, J. E. Kinsey, T. C. Luce, K. H. Burrell, D. R. Baker, E. J. Doyle, X. Garbet, R. A. Moyer, C. L. Rettig, T. L. Rhodes, D. W. Ross, G. M. Staebler, R. Sydora, and M. R. Wade, *Nucl. Fusion* **41**, 1235 (2001).

¹⁹R. D. Durst, R. J. Fonck, G. Cosby, and H. Evensen, *Rev. Sci. Instrum.* **63**, 4921 (1992).

²⁰R. J. Groebner, K. H. Burrell, and R. P. Seraydarian, *Phys. Rev. Lett.* **64**, 3015 (1990).

²¹J. A. Boedo, D. Rudakov, R. Moyer, S. Krashennikov, D. Whyte, G. McKee, G. Tynan, M. Schaffer, P. Stangeby, P. West, S. Allen, T. Evans, R. Fonck, E. Hollmann, A. Leonard, A. Mahdavi, G. Porter, M. Tillack, and G. Antar, *Phys. Plasmas* **8**, 4826 (2001).

²²R. J. Groebner, T. H. Osborne, A. W. Leonard, and M. E. Fenstermacher, *Nucl. Fusion* **49**, 045013 (2009).

²³E. Wolftrum, A. Burckhart, R. Fischer, N. Hicks, C. Konz, B. Kurzan, B. Langer, T. Pütterich, H. Zohm, and the ASDEX Upgrade Team, *Plasma Phys. Controlled Fusion* **51**, 124057 (2009).

²⁴B. Kurzan, E. Wolftrum, A. Burckhart, T. Pütterich, B. Wieland, R. Fischer, P. Schneider, W. Suttrop, and H. Zohm, Proceedings of the 23rd IAEA Fusion Energy Conference, Daejeon, Republic of Korea, 2010, Paper EXC/P3-03, http://www-pub.iaea.org/mtcd/meetings/cn180_papers.asp

²⁵A. Burckhart, E. Wolftrum, R. Fischer, K. Lackner, H. Zohm, and the ASDEX Upgrade Team, *Plasma Phys. Controlled Fusion* **52**, 105010 (2010).

²⁶W. Dorland, F. Jenko, M. Kotschenreuther, and B. N. Rogers, *Phys. Rev. Lett.* **85**, 5579 (2000).

²⁷R. J. Groebner, T. H. Osborne, M. E. Fenstermacher, A. W. Leonard, M. A. Mahdavi, P. B. Snyder, and D. M. Thomas, in *Proceedings of the 31st EPS Conference on Plasma Physics, London, 28 June–2 July 2004*, Vol. 28G (ECA) P-2.173. http://epsppd.epfl.ch/London/pdf/P2_173.pdf

²⁸J. Neuhauser, D. Coster, H. U. Fahrbach, J. C. Fuchs, G. Haas, A. Herrmann, L. Horton, M. Jakobi, A. Kallenbach, M. Laux, J. W. Kim, B. Kurzan, H. W. Müller, H. Murmann, R. Neu, V. Rohde, W. Sandmann, W. Suttrop, E. Wolftrum, and the ASDEX Upgrade Team, *Plasma Phys. Controlled Fusion* **44**, 855 (2002).

²⁹J. W. Hughes, B. LaBombard, J. Terry, A. Hubbard, and B. Lipschultz, *Nucl. Fusion* **47**, 1057 (2007).

³⁰F. Jenko, D. Told, P. Xanthopoulos, F. Merz, and L. D. Horton, *Phys. Plasmas* **16**, 055901 (2009).

³¹J. D. Callen, *Phys. Rev. Lett.* **94**, 055002 (2005).

³²R. Maingi, M. G. Bell, E. D. Fredrickson, K. C. Lee, R. J. Maqueda, P. Snyder, K. Tritz, S. J. Zweben, R. E. Bell, T. M. Biewer, C. E. Bush, J. Boedo, N. H. Brooks, L. Delgado-Aparicio, C. W. Domier, D. A. Gates, D. W. Johnson, R. Kaita, S. M. Kaye, H. W. Kugel, B. P. LeBlanc, N. C. Luhmann, J. E. Menard, D. Mueller, H. Park, R. Raman, A. L. Roquemore, S. A. Sabbagh, V. A. Soukhanovskii, T. Stevenson, and D. Stutman, *Phys. Plasmas* **13**, 092510 (2006).